Chinese Chemical Letters 36 (2025) 110058

Contents lists available at ScienceDirect

Chinese Chemical Letters

journal homepage: www.elsevier.com/locate/cclet

Cerium-based metal-organic framework-modified natural mineral vermiculite for photocatalytic nitrogen fixation under visible-light irradiation

Sixiao Liu, Tianyi Wang*, Lei Zhang, Chengyin Wang, Huan Pang*

College of Chemistry and Chemical Engineering, Yangzhou University, Yangzhou 225002, China

ARTICLE INFO

Article history:
Received 23 October 2023
Revised 25 May 2024
Accepted 27 May 2024
Available online 27 May 2024

Keywords:
Metal-organic frameworks
Vermiculite
Nitrogen fixation
Visible-light
Low-cost

ABSTRACT

In order to protect the environment and economize energy, a nitrogen-fixing photocatalyst, VMCeact, is investigated in this work. This catalyst is prepared from a natural mineral, vermiculite, and modified by Ce-based metal-organic framework, Ce-UiO-66. Vermiculite was treated with formic acid; thus, Ce-UiO-66 particles grew *in-situ* on vermiculite; then, Ce-UiO-66 particles were activated by ultraviolet irradiation. The vermiculite absorbed visible light with a narrow band gap, and transferred photogenerated electrons to the active sites on Ce-UiO-66. Moreover, the lamella structure of vermiculite protected Ce-UiO-66 during photocatalytic process. Therefore, with only 45.92 wt% of Ce-UiO-66, the nitrogen fixation performance of VMCeact was 2.29 times that of pure activated Ce-UiO-66 particles under 455 nm light irradiation (apparent quantum efficiency of 4.49%), and retained at least 96.05% performance after 7 × 24 h of photocatalytic reaction. This cost-reduced, efficient and stable photocatalyst has the opportunity to facilitate environmentally friendly ammonia production.

Ammonia is an important industrial material and the primary raw material for nitrogen fertilizers. Therefore, artificial ammonia is in high demand around the whole world. Ammonia is produced by the Haber-Bosch process, which synthesizes nitrogen and hydrogen into ammonia with thermal catalysts [1,2]. However, the Haber-Bosch process suffers from high energy requirements (300–500 °C, 15–30 MPa), and its efficiency is limited to 10%−15%. Nowadays, approximately 1.4% of global energy is consumed for nitrogen fixation [3-5]. Thereby, it is necessary to develop sustainable nitrogen fixation processes, including the photocatalytic nitrogen fixation process, which converts N_2 and H_2O to NH_3 under light irradiation [6-10]. The application of photocatalytic nitrogen fixation is currently disadvantaged by its insufficient efficiency and expensive raw materials. Therefore, effective and inexpensive photocatalysts are aimed in the study of nitrogen fixation. In this investigation, a cost-effective natural material, vermiculite, was modified to address these issues.

Many modified materials have shown the advantages of photocatalytic nitrogen fixation, such as TiO_2, Fe_2O_3, and C_3N_4 [9-15]. Among them, the MOFs (metal-organic frameworks) photocatalysts take advantages of porous structure, adjustable metal centers and organic ligands, and high crystallinity [16-22]. Ce-based MOF, Ce-UiO-66, takes the advantages of forming nitrogen fixation active sites under ultraviolet light irradiation in the previous research of our group [23]. Moreover, Ce-UiO-66 has disadvantages such as low visible-light absorption, high cost, and poor stability, which could potentially be improved by loading it with vermiculite (VMT) in this investigation.

Vermiculite is a porous, inexpensive, nontoxic, lightweight, and obtainable natural mineral [14,24], even may be widespread on Mars [25]. And vermiculite is a monoclinic crystal, and the chemical formula is $(Mg, Fe, Al)_3[(Si, Al)_4O_{10}(OH)_2]\cdot 4H_2O$. As a layered silicate mineral, the unit layer of vermiculite is composed of tetrahedral and octahedral elements in a 2:1 ratio, with a thickness of approximately 1 nm. Due to its unique layered structure, expandability, and high adsorption capacity, vermiculite shows great potential as a photocatalyst material for degrading organic pollutants (including Rhodamine B, methylene, brilliant orang X-GN, tetracycline, and phenol) [24,26-29] and hydrogen production [30,31]. Herein, vermiculite is used in nitrogen fixation photocatalyst for the first time.

A nitrogen fixation photocatalyst VMCeact is reported in this paper, which was prepared by loading ultraviolet-activated Ce-UiO-66 particles on formic acid-treated vermiculite. Vermiculite has a

* Corresponding authors.
E-mail addresses: wangty@yzu.edu.cn (T. Wang), panghuan@yzu.edu.cn (H. Pang).

https://doi.org/10.1016/j.cclet.2024.110058
1001-8417/

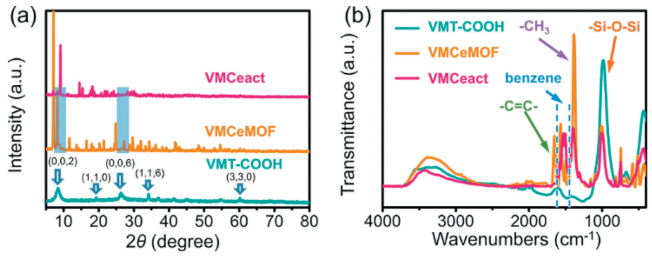

Fig. 1. (a) XRD pattern of VMT-COOH, VMCeMOF, and VMCeact. (b) FT-IR pattern of VMT-COOH, VMCeMOF, and VMCeact.

narrow band gap that allows it to absorb visible light. Thus, photogenerated electrons are transferred from vermiculite to active sites on Ce-UiO-66 particles for nitrogen fixation. Furthermore, vermiculite provides protection to Ce-UiO-66 particles [32,33] due to its layered structure. Ce-UiO-66 particles were grown on the surface of vermiculite in order to taking advantage of active sites from Ce-UiO-66, and the layered vermiculite is able to avoid collision and friction of MOFs particles. Consequently, VMCeact exhibited remarkable and stable nitrogen fixation performance under visible light irradiation, and the cost of photocatalyst was significantly reduced.

The crystal structures of VMT-COOH, VMCeMOF, and VMCeact were characterized by X-ray diffraction (XRD) and the results are shown in Fig. 1a. The pretreated vermiculite VMT-COOH showed four main characteristic peaks at 8.42°, 19.37°, 26.49°, and 34.23° The characteristic peaks at 8.42° and 26.49° represented the (002) and (006) crystal planes of vermiculite (PDF #74–1732 and PDF #00–050–0459), which are layer planes of dehydrated vermiculite [34]. These peaks proved that VMT-COOH remained a layered structure and the relatively large FWHMs (full width at half maxima) of these peaks indicated that the distances between layers were not uniform. The other two characteristic peaks were from the silicate crystals of vermiculite. After the *in-situ* growth of Ce-UiO-66 particles, VMCeMOF showed characteristic peaks of the Ce-UiO-66 structure, including the two main peaks at 7.13° and 8.23° (Fig. S1 in Supporting information). The small FWHMs of these characteristic peaks proved the high crystallinity of Ce-UiO-66 particles. The (002) and (006) crystal planes of vermiculite were detected in the XRD spectra of VMCeMOF, which indicated the layered structure of vermiculite was maintained after Ce-UiO-66-loading. After ultraviolet activation, VMCeact exhibited a new characteristic peak at 9.15° and weaker peaks at 7.13° and 8.23°. This phenomenon proved the successful activation of Ce-UiO-66 particles, that is, the breakage of benzene-C bonds and the formation of active sites for nitrogen fixation [23]. Moreover, these peaks of (002) and (006) crystal planes of vermiculite also decreased in the XRD spectra of VMCeact, while the result of FT-IR (Fourier transform infrared measurements) (Fig. 1b and Fig. S2 in Supporting information) confirmed that vermiculite was still the main component of VMCeact. Thus, the result of XRD was interpreted as Ce-UiO-66 particles were not sandwiched between the layers of vermiculite, which avoided the underutilization of active sites on Ce-UiO-66 particles.

The structure of VMT-COOH, VMCeMOF, and VMCeact were also characterized by FT-IR and the results are shown in Fig. 1b. The peaks in the region of 3500–3000 cm^{-1} represented the stretching vibrations of O–H and C–H. The peak of VMT-COOH in this region was relatively wide due to the loading of carboxyl groups after pretreatment, The peaks of VMCeMOF and VMCeact in this region narrowed and red-shifted, indicating the decrease of carboxyl groups and the crystallization of Ce-UiO-66. All these samples showed a strong peak at 1000 cm^{-1}, which represented the

Table 1
The contents of metal elements in VMT-COOH.

Element	Si	Fe	Al	Mg	K
Weight (%)	8.22	8.67	3.96	4.80	3.02
Atomic (%)	5.64	2.99	2.83	3.80	1.49

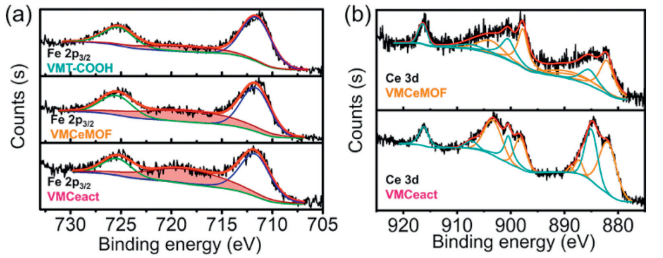

Fig. 2. (a) XPS Fe $2p_{3/2}$ spectra of VMT-COOH, VMCeMOF, and VMCeact. (b) XPS Ce 3d spectra of VMCeMOF and VMCeact.

bonds of -Si-O-Si- in the vermiculite structure. Therefore, vermiculite was proved to be the main component of VMCeMOF and VMCeact. The other main peaks were the bending vibration peak of $-CH_3$ at 1380 cm^{-1}, the stretching vibration peak group of benzene rings at 1620–1450 cm^{-1}, and the stretching vibration peak of -C=C- at 1653 cm^{-1}. VMCeMOF and VMCeact both showed strong $-CH_3$ peaks, which belonged to ligands in Ce-UiO-66 (H_2BDC) [35]. Compared to VMCeMOF, VMCeact showed stronger stretching vibration peaks of benzene rings, while its stretching vibration peak of -C=C- decreased. This phenomenon proved the breakages of benzene-C bonds on Ce-UiO-66 particles due to the vibration of benzene rings and -C=C- bonds were changed after ultraviolet activation. Furthermore, the out-of-plane bending vibration peak of C–H at 1000-650 cm^{-1} remained after ultraviolet activation, indicating that the substitution of benzene rings did not change and the active sites were formed in the ligands of Ce-UiO-66 particles.

The mass ratio of vermiculite was analyzed by EDX (Energy Dispersive X-ray) and the result is shown in Table 1. The contents of Si, Al and Fe in VMT-COOH were higher than that of Mg and K. According to the narrow band gap of VMT-COOH, the crystal structure of iron oxide with a narrow band gap in vermiculite was considered to be the source of its semiconductor characteristic.

The electronic states of Fe and Ce were characterized by X-ray photoelectron spectroscopy (XPS) and the XPS Fe $2p_{3/2}$ spectra is shown in Fig. 2a. Three peaks were detected in VMT-COOH, VMCeMOF and VMCeact, including peaks of Fe^{3+} at 711.6 eV and 725.3 eV, and the satellite peak of Fe^{3+} at 718.4 eV [36-38]. This result indicated that Fe atoms in the vermiculite were trivalent, and the valence state of Fe was not altered by *in-situ* growth or ultraviolet activation. Moreover, the area of Fe^{3+} satellite peak relatively increased after *in-situ* growth and ultraviolet activation (specific peak areas are shown in Table S1 in Supporting information). Since the valence state of Fe was not altered, the reason for the change in peak areas were considered to be signal reception of XPS. The signal reception of Fe $2p_{3/2}$ with high spin was affected by the ligands of iron oxide with electronegativity. In this investigation, Ce-UiO-66 particles with electronegativity were loaded on VMT-COOH; hence, VMCeMOF showed a relatively stronger satellite peak. After ultraviolet activation, electron-rich active sites were formed on Ce-UiO-66 particles and the electronegativity of Ce-UiO-66 particles increased, thus the satellite peak area of VMCeact was further increased. The changes of electronegativity proved that the trend of electron transfer was from vermiculite to Ce-UiO-66 particles. The XPS Ce 3d spectra (Fig. 2b) indicated that the peak areas of Ce^{3+} decreased relatively (specific peak areas are shown in Table S2 in Supporting information, and XPS Si 2p spectra and XPS Al 2p

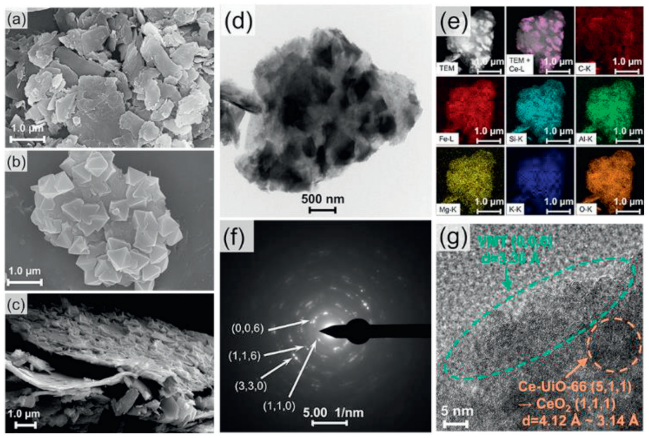

Fig. 3. SEM images of (a) VMT-COOH, (b) VMCeMOF, and (c) VMCeact. (d) TEM image, (e) TEM-mapping images, (f) SAED image, (g) HR-TEM image of VMCeact.

spectra are shown in Fig. S3 in Supporting information). This result proved that no oxygen vacancies were formed on the surface of Ce-UiO-66 particles after ultraviolet activation. In the characterization of EPR (Electron paramagnetic resonance) (Fig. S4 in Supporting information), no peaks of oxygen vacancies were received near $g = 2.00$. According to these results, oxygen vacancies on cerium clusters of Ce-UiO-66 particles or iron oxide of vermiculite were excluded to be active site in this investigation.

The morphologies of VMT-COOH, VMCeMOF, and VMCeact were characterized by scanning electron microscope (SEM), transmission electron microscope (TEM) and high resolution TEM (HR-TEM), and the images are shown in Fig. 3. The pretreated vermiculite VMT-COOH exhibited layered morphology with a diameter of 1–10 μm in Fig. 3a. Octahedral Ce-UiO-66 particles were grown *in-situ* on the surface of VMT-COOH in Fig. 3b. After ultraviolet activation, Ce-UiO-66 particles exhibited the activated morphology and were stably loaded on the surface of VMCeact in Fig. 3c. Furthermore, two shades of colors were observed in the TEM image of VMCeact (Fig. 3d), including the layer structure with more electron beam penetration and the particle structure with less electron beam penetration. The element distribution of VMCeact was analyzed by TEM-mapping [39,40] and the result is shown in Fig. 3e. The layer structure was uniformly distributed with Fe, Si, Al, Mg, K, and O, which was consistent with the characteristics of vermiculite. The particle structure was distributed with Ce element, which was consistent with Ce-UiO-66. Then the structural composition of VMCeact was further confirmed by selected area electron diffraction (SAED). Some circles formed with multiple bright spots were shown in the SAED image (Fig. 3f). These circles represented the (110), (006), (116), and (330) crystal planes of vermiculite, respectively, and the calculated data are shown in Table S3 (Supporting information). Moreover, these bright spots did not form uniform circles, which implied the crystal of vermiculite in VMCeact was oriented. This phenomenon was consistent with the natural layered structure of vermiculite. Two different lattice planes were exhibited in the HR-TEM image (Fig. 3g). The lattice plane at the edge of VMCeact was 3.36 Å, corresponding to the (006) crystal plane of vermiculite. The lattice plane was displayed to 4.12 Å ~ 3.14 Å on the inner of VMCeact, corresponding to the (511) crystal plane of Ce-UiO-66 and the (111) crystal plane of CeO_2 clusters. The results of SEM and TEM demonstrated that the morphology of VMCeact was layered vermiculite with Ce-UiO-66 particles loading on the surface.

The absorption performances of samples were characterized by UV–vis (Ultraviolet and Visible Spectrophotometry), as shown in Fig. 4a. VMT-COOH exhibited strong visible light absorption, resulting in a brownish black color. VMCeMOF showed stronger UV

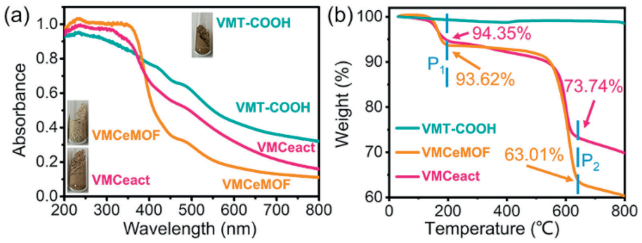

Fig. 4. (a) UV–vis spectra and images of VMT-COOH, VMCeMOF, and VMCeact. (b) TGA curves of VMT-COOH, VMCeMOF, and VMCeact.

absorption and weaker visible light absorption, resulting in a light-yellow color, due to the Ce-UiO-66 particles were uniformly loaded on the surface of vermiculite (Fig. 3) and Ce-UiO-66 only absorbed light with a wavelength below 400 nm (Fig. S5 in Supporting information). After ultraviolet activation, the visible light absorption of Ce-UiO-66 increased and the electron exchange between vermiculite and Ce-UiO-66 particles increased (XPS Fe), thus the visible light absorption of VMCeact enhanced and exhibited a brownish-gray color. According to the result of TGA (Thermogravimetric Analysis) in Fig. 4b, the mass ratios of Ce-UiO-66 in VMCeMOF and VMCeact were 68.76 wt% and 45.92 wt%, respectively.

The cycling ammonia generations of VMCeact under the irradiation of ultraviolet light or visible light were tested in the performance experiments, and the results are shown in Fig. 5a. The ammonia generation of VMCeact under ultraviolet light was tested by an LED lamp with a wavelength of 365 nm, and the light intensity received by the reactor was 3.5 mW/cm^2. The ammonia generation of VMCeact under visible light was tested by an LED lamp with a wavelength of 455 nm, and the light intensity received by the reactor was also 3.5 mW/cm^2. In the first 24 h reaction, VMCeact generated 2.28 mmol/L ammonia under UV irradiation, and 1.86 mmol/L ammonia under visible light irradiation. VMCeact showed excellent stability after 7 × 24 h photocatalytic reaction. VMCeact maintained 96.05% of photocatalytic performance under UV irradiation and 97.45% of photocatalytic performance under visible light irradiation, while pure Ce-UiO-66 particles were completely inactivated (the cycling performance of activated Ce-UiO-66 particles is shown in Fig. S6 (Supporting information), and the ammonia concentrations were also tested by chromogenic method (Fig. S7 in Supporting information). The result indicated that loading on vermiculite

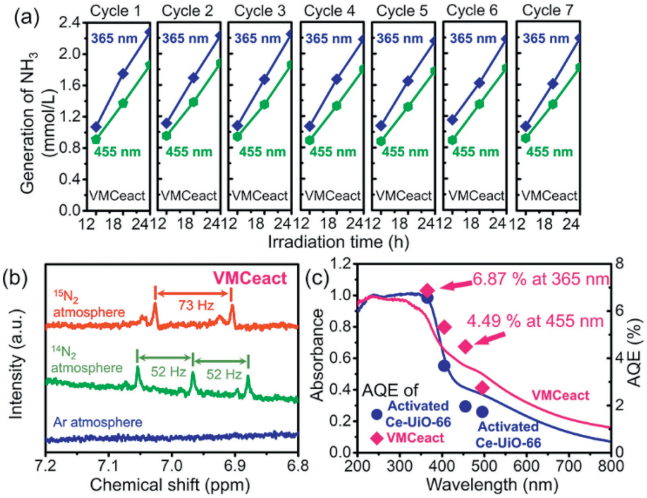

Fig. 5. (a) NH_3 generation of VMCeact in 7 cycles under 365 nm light or 455 nm light irradiation. (b) ^{1}H spectra of the product liquid from VMCeact in different atmospheres. (c) AQEs of activated Ce-UiO-66 and VMCeact.

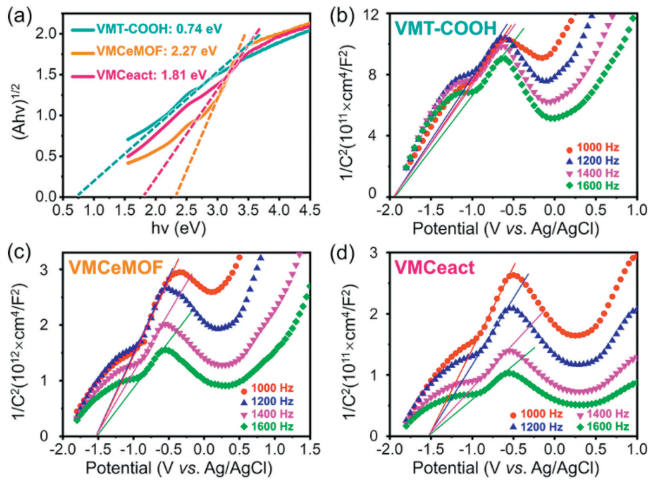

Fig. 6. (a) Optical band gaps of VMT-COOH, VMCeMOF, and VMCeact. Flat band potentials of (b) VMT-COOH, (c) VMCeMOF, and (d) VMCeact.

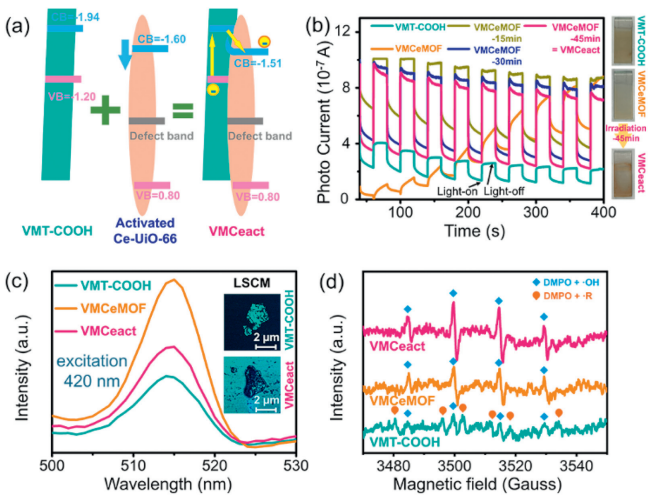

Fig. 7. (a) Band structure of VMCeact. (b) *in-situ* photocurrent curves of VMT-COOH and VMCeMOF→VMCeact. (c) FL spectra and LSCM images of VMT-COOH, VMCeMOF, and VMCeact. (d) Free radical EPR spectra of VMT-COOH, VMCeMOF, and VMCeact.

controlled the activation of Ce-UiO-66 particles and the layered structure of vermiculite avoided the mechanical damage of Ce-UiO-66 particles during the reaction.

In order to discuss the source of ammonia, a $^{15}N_2$ atmosphere, a $^{14}N_2$ atmosphere, and an Ar atmosphere were utilized in the photocatalytic reaction, respectively. The ^1H spectra of the product liquid were obtained by NMR. The peaks of a triplet state with $J(N–H) = 52$ Hz should be observed in the ^1H spectra if the product were $^{14}NH_4^+$; the peaks of a double state with $J(N–H) = 73$ Hz should be observed in the ^1H spectra if the product were $^{15}NH_4^+$. As a result, in Fig. 5b, VMCeact produced $^{14}NH_4^+$ in the $^{14}N_2$ atmosphere (ordinary nitrogen) and produced $^{15}NH_4^+$ in the $^{15}N_2$ atmosphere (isotopic labeled nitrogen). The $^{14}NH_4^+$ or $^{15}NH_4^+$ were not produced in the Ar atmosphere. Therefore, the nitrogen in water was proved to be the source of ammonia in the photocatalytic nitrogen fixation of VMCeact.

The performance of VMCeact under ultraviolet or visible light irradiation was systematically reflected by the AQE (apparent quantum efficiency) of photocatalytic nitrogen fixation, as shown in Fig. 5c. VMCeact showed an AQE of 6.87% under 365 nm light irradiation, which was similar to the AQE of pure activated Ce-UiO-66 (ultraviolet activated pure Ce-UiO-66 particles). Meanwhile, VMCeact showed the AQE of 4.49%, while the AQE of pure activated Ce-UiO-66 was only 1.96%. Under the irradiation of visible light, VMCeact exhibited significantly higher AQE than pure activated Ce-UiO-66 (2.29 times), which was consistent with the absorption of these samples. The result of AQE proved that the photocatalytic performance of Ce-UiO-66 was improved by loading onto vermiculite with only 45.92 wt% of Ce-MOF material.

The advantages of VMCeact were discussed by band structure and electron transfer. The optical band gaps of samples were calculated from UV–vis spectra and Tauc plots and the result is shown in Fig. 6a. VMT-COOH showed a very narrow band gap of 0.74 eV, while Ce-UiO-66 loaded VMCeMOF showed a wider gap of 2.27 eV due to the band gap of Ce-UiO-66 particles have a 2.57 eV band gap (Fig. S8 in Supporting information). Ultraviolet activated VMCeact showed the optical band gap of 1.81 eV because the band gap of Ce-UiO-66 particles narrowed after activation (Fig. S8).

The Mott-Schottky equation was utilized to measure samples in order to further explore the band structure of VMCeact. The flat band potentials of samples were exhibited in Figs. 6b-d, which are the positions where the extension of straight part in Mott-Schottky curve intersected on the X-axis. The flat band potentials reflected the conduction band (CB) positions of VMT-COOH, VMCeMOF and VMCeact, since both vermiculite and Ce-UiO-66 are n-type semiconductors (their total slopes of Mott-Schottky curve were positive), and the CB of Ce-UiO-66 and activated Ce-UiO-66 are shown in Fig. S9 (Supporting information). The CB of VMT-COOH was located at −1.94 eV The CB of VMCeMOF and VMCeact are both located at −1.51 eV, while the CB of Ce-UiO-66 and activated Ce-UiO-66 are 2.55 eV and 2.30 eV respectively.

The transfer of CB positions proves that band bending appears between vermiculite and Ce-UiO-66. Thus, the band structure of VMCeact was simulated based on the characterizations above, as shown in Fig. 7a. And the change of the band structure during the preparation process is shown in Fig. S10 (Supporting information). The valence bands (VB) of vermiculite were obtained by the formula: VB = optical band gap – CB, and the VB of Ce-UiO-66 particles were characterized by XPS-VBM (Fig. S11 in Supporting information), due to a defect band formed in Ce-UiO-66 after UV-irradiation. The activated Ce-UiO-66 formed a defect band after UV-activation due to the breakage of benzene-C bonds, which narrowed the optical band gaps of activated Ce-UiO-66 and VMCeact. According to the results of CB characterization, the CB position of VMCeact was lower than that of activated Ce-UiO-66, which demonstrated that the CB band of Ce-UiO-66 particles in VMCeact bended upward. The result proved that photogenerated electrons transferred from vermiculite to Ce-UiO-66 particles, which was also consistent with the increase of peak area at 718.4 eV in Fig. 1c (XPS Fe $2p_{3/2}$). Therefore, vermiculite absorbs visible light with a narrow band gap, and then transfers photogenerated electrons to Ce-UiO-66. The unique band structure increased the generation and utilization efficiency of electrons during the photocatalytic reaction, which took advantage in the nitrogen fixation performance, as shown in Fig. 5. Furthermore, the generation and utilization efficiency of electrons was characterized by the following experiments.

The activation process and electron transfer of VMCeact were analyzed by *in-situ* photocurrent measure under the irradiation of a Xe lamp (full wavelength) [41], and the result is shown in Fig. 7b. VMT-COOH showed stable photocurrent intensity of 1.06×10^{-7} A. The photocurrent intensity of VMCeMOF increased with the light irradiation, that proved activation increased the photogenerated electrons of VMCeMOF. After 45 min of light irradiation, the photocurrent intensity stabilized, that is, VMCeMOF was activated into VMCeact. The photocurrent intensity of VMCeact was 5.26×10^{-7} A, which was five times of that of vermiculite and similar to that of equal Ce-UiO-66 particles (Ce-UiO-66 was activated by 30 min

light irradiation in Fig. S12 (Supporting information), of activated Ce-UiO-66 in VMCeact). Therefore, the photocatalytic performance of VMCeact was increased according to the photogenerated electrons of VMCeact were increased by Ce-UiO-66-loading.

The electron-hole recombination of VMCeact was analyzed by FL (Fluorescence emission measurement) and LSCM (Laser Scanning Confocal Microscopy), and the result is shown in Fig. 7c. FL was characterized under the excitation light with a wavelength of 420 nm. VMCeMOF showed the highest fluorescence intensity, while VMT-COOH and VMCeact showed lower fluorescence intensities. The low FL intensity of VMT-COOH was due to its lower number of photogenerated electrons from vermiculite. The FL intensity of VMCeact was lower than that of VMCeMOF due to more effective electron transfer and increased electrons consumption in nitrogen fixation. The effective electron transfer of VMCeact was proved by the characterization of XPS (Fig. 2a), band structure (Fig. 7a), and photocurrent (Fig. 7b). Moreover, active sites for nitrogen fixation were formed by activation on Ce-UiO-66 particles, that increased the consumption of election by reducing nitrogen molecules [15]. The recombination of electrons and holes was intuitively analyzed by the LSCM images in Fig. 7c and Fig. S13 (Supporting information). The VMT-COOH particles exhibited textured fluorescence under the irradiation of 420 nm × 2 (two-photon with the penetration depth of 1 mm), while fluorescence was not detected on the Ce-UiO-66 loaded position of the VMCeact particle. The recombination of electrons and holes generate fluorescence, thus, the distribution of fluorescence in LSCM images characterize the position of electro-hole recombination [42,43]. The result of LSCM further proved that the recombination of electrons and holes was decreased by Ce-UiO-66-loading.

The oxidation reaction of VMCeact during photocatalytic nitrogen fixation was analyzed by free radical characterization of EPR, and the result is shown in Fig. 7d and Fig. S14 (Supporting information). The peaks of hydroxyl radicals (•OH) and carbon center radicals (•R) were detected in the EPR spectra of VMT-COOH. •R was generated from the carboxyl groups on VMT-COOH [44,45], and •OH was generated by oxidizing H_2O from the structure of Fe_2O_3 in vermiculite [46]. Moreover, only peaks of •OH were distinguished in the EPR spectra of VMCeMOF and VMCeact. The disappearance of •R demonstrated that none carboxyl groups remained on VMCeMOF or VMCeact, and •OH was generated by oxidizing H_2O. Furthermore, the peak intensity of VMCeact was higher than that of VMCeMOF. This result proved that the advantageous electron transfers of VMCeact not only improved the performance of nitrogen fixation on its CB, but also oxidized more H_2O on its VB, thus VMCeact generated more NH_3 in the performance experiments. In summary, according to the high visible light absorption and advantageous photogenerated electron transfers, low-cost VMCeact exhibited a remarkable photocatalytic performance for nitrogen fixation under visible light irradiation.

To summarize, a nitrogen fixation photocatalyst, VMCeact, was investigated in this work, which was prepared by *in-situ* growing Ce-UiO-66 on the formic acid-treated vermiculite. The layered structure of vermiculite significantly improved the stability of VMCeact and maintained a minimum of 96.05% performance after 7 × 24 h of photocatalytic reaction, while pure Ce-UiO-66 particles were completely inactivated. Moreover, vermiculite showed the advantages of visible light absorption and photogenerated electron transfer. Hence, VMCeact exhibited outstanding AQE of 4.49% under the irradiation of visible light (455 nm) with only 45.92 wt% of Ce-UiO-66, which was 1.29 times higher than the AQE of pure activated Ce-UiO-66. Therefore, VMCeact, derived from low-cost natural mineral, exhibited remarkable photocatalytic nitrogen fixation performance and high stability under the irradiation of visible light.

Declaration of competing interest

The authors declare that they have no known competing financial interests or personal relationships that could have appeared to influence the work reported in this paper.

CRediT authorship contribution statement

Sixiao Liu: Writing – original draft. **Tianyi Wang:** Writing – review & editing. **Chengyin Wang:** Writing – review & editing. **Huan Pang:** Writing – review & editing.

Acknowledgments

This study was supported by the National Natural Science Foundation of China (Nos. 21978251, 22102141 and U1904215) and Natural Science Foundation of Jiangsu Province (No. BK20200044).

Supplementary materials

Supplementary material associated with this article can be found, in the online version, at doi:10.1016/j.cclet.2024.110058.

References

[1] J.W. Erisman, M.A. Sutton, J. Galloway, Z. Klimont, W. Winiwarter, Nat. Geosci. 1 (2008) 636–639.
[2] H. Liu, Chin. J. Catal. 35 (2014) 1619–1640.
[3] C.J. van der Ham, M.T. Koper, D.G. Hetterscheid, Chem. Soc. Rev. 43 (2014) 5183–5191.
[4] C. Smith, A.K. Hill, L. Torrente-Murciano, Energy Environ. Sci. 13 (2020) 331–344.
[5] K. Honkala, A. Hellman, I.N. Remediakis, et al., Science 307 (2005) 555–558.
[6] X. Chen, N. Li, Z. Kong, W.J. Ong, X.J. Zhao, Mater. Horiz. 5 (2018) 9–27.
[7] A.J. Medford, M.C. Hatzell, ACS Catal. 7 (2017) 2624–2643.
[8] G. Qing, R. Ghazfar, S.T. Jackowski, et al., Chem. Rev. 120 (2020) 5437–5516.
[9] R. Li, Chin. J. Catal. 39 (2018) 1180–1188.
[10] S. Chen, D. Liu, T. Peng, Sol. RRL 5 (2020) 2000487.
[11] S. Zhang, Y. Zhao, R. Shi, G.I.N. Waterhouse, T.R. Zhang, EnergyChem 1 (2019) 100013.
[12] S. Lin, X. Zhang, L. Chen, et al., Green Chem. 24 (2022) 9003–9026.
[13] L. Zhang, S. Hou, T. Wang, et al., Small 18 (2022) e2202252.
[14] Z. Xing, J. Zhang, J. Cui, et al., Appl. Catal. B 225 (2018) 452–467.
[15] W. Zhao, J. Zhang, X. Zhu, et al., Appl. Catal. B 144 (2014) 468–477.
[16] S.L. Li, Q. Xu, Energy Environ. Sci. 6 (2013) 1656–1683.
[17] B. Zhu, R. Zou, Q. Xu, Adv. Energy Mater. 8 (2018) 1801193.
[18] L. Fan, Q. Yu, J. Chen, et al., Catalysts 12 (2022) 1005.
[19] Y.B. Huang, J. Liang, X.S. Wang, C. Rong, Chem. Soc. Rev. 46 (2017) 126–157.
[20] H. Furukawa, K.E. Cordova, M. O'Keeffe, O.M. Yaghi, Science 341 (2013) 1230444.
[21] J.D. Xiao, R. Li, H.L. Jiang, Small Methods 7 (2023) e2201258.
[22] Y. Liu, X. Ye, R. Li, et al., Chin. Chem. Lett. 33 (2022) 5162–5168.
[23] S. Liu, Z. Teng, H. Liu, et al., Angew. Chem. Int. Ed. Engl. 61 (2022) e202207026.
[24] C. Huang, S. Zhang, M. Wang, et al., Appl. Clay Sci. 213 (2021) 106242.
[25] J. Cuadros, C. Mavris, J.R. Michalski, Appl. Clay Sci. 228 (2022) 106643.
[26] C. Tang, M. Hu, M. Fang, et al., Nanoscale Res. Lett. 10 (2015) 276.
[27] E. Fan, F. Hu, W. Miao, et al., Appl. Clay Sci. 197 (2020) 105789.
[28] E. Fan, H. Xu, S. Sun, et al., Colloids Surf. A 669 (2023) 131510.
[29] Q. Chen, P. Wu, Z. Dang, et al., Sep. Purif. Technol. 71 (2010) 315–323.
[30] M. Reli, N. Ambrožová, M. Valášková, et al., Energy Convers. Manage. 238 (2021) 114156.
[31] M. Valášková, K. Kočí, J. Madejová, et al., Minerals 12 (2022) 607.
[32] L.R. Redfern, O.K. Farha, Chem. Sci. 10 (2019) 10666–10679.
[33] M. Lammert, C. Glissmann, N. Stock, Dalton. Trans. 46 (2017) 2425–2429.
[34] L. Ma, X. Su, Y. Xi, et al., Appl. Clay Sci. 183 (2019) 105332.
[35] Y. Yan, Y. Chu, M.A. Khan, et al., Sci. Total. Environ. 806 (2022) 150652.
[36] A.D. Purceno, A.P.C. Teixeira, A.B. Souza, et al., Appl. Clay Sci. 69 (2012) 87–92.
[37] S. More, S. Raut, S. Premkumar, et al., RSC Adv. 10 (2020) 32088–32101.
[38] A.P. Grosvenor, B.A. Kobe, M.C. Biesinger, N.S. Mclntyre, Surf. Interface Anal. 36 (2004) 1564–1574.
[39] Y. Wang, Q. Li, W. Shi, P. Cheng, Chin. Chem. Lett. 31 (2020) 1768–1772.
[40] P. Jing, B. Wu, Z. Han, W. Shi, P. Cheng, Chin. Chem. Lett. 32 (2021) 3505–3508.
[41] N. Liu, J. Jiang, Z. Chen, et al., Angew. Chem. Int. Ed. 62 (2023) e202312306.
[42] P. Wang, L. Tian, X. Gao, Y. Xu, P. Yang, ChemCatChem 12 (2020) 4185–4197.
[43] F. Gao, Q. Liao, Z.Z. Xu, et al., Angew. Chem. Int. Ed. 49 (2010) 732–735.
[44] Y. Nosaka, A.Y. Nosaka, Chem. Rev. 117 (2017) 11302–11336.
[45] L. Chen, J. Duan, P. Du, et al., Water Res. 221 (2022) 118747.
[46] Q.F. Bao, M. Li, Y. Xia, et al., Org. Lett. 23 (2021) 1107–1112.